ACS NANO

www.acsnano.org

ARTICLE

Dynamic Response of Concentrated Electrolytes to Chirp Signals

Emily Krucker-Velasquez,* Martin Z. Bazant, Alfredo Alexander-Katz, and James W. Swan

Cite This: *ACS Nano* 2025, 19, 13673−13684

Read Online

ACCESS | Metrics & More | Article Recommendations | Supporting Information

ABSTRACT: **Electrolytes, chirp signals, Brownian dynamics, conductivity, Maxwell−Wagner relaxation This study investigates the dynamic response of electrolyte/macroion solutions to time-varying electric fields, which is vital for applications from water desalination to neuromorphic computing and sensor technologies. Using large-scale Brownian dynamics simulations coupled with Poisson's equation, we examined the frequency-dependent conductivity of symmetric and binary electrolytes/nanoparticles across various concentrations. We reveal a comprehensive picture of charge transport mechanisms by employing chirp signals that excite multiple frequencies. Our results identify three distinct dynamic regimes: (1) instantaneous response at low frequencies, (2) increased lagging and imaginary conductivity at intermediate frequencies, and (3) diminished conductivity at high frequencies due to short-time ion/macroion dynamics. Significant deviations from ideal behavior at low frequencies and high concentrations are attributed to packing and many−body interactions. We propose a modified Maxwell−Wagner relaxation time that incorporates excluded volume effects, offering a more accurate time scale for the dynamic response of concentrated electrolytes/macroions. This new framework scales the frequency-dependent conductivity, revealing universal responses across different concentrations and interaction strengths.**

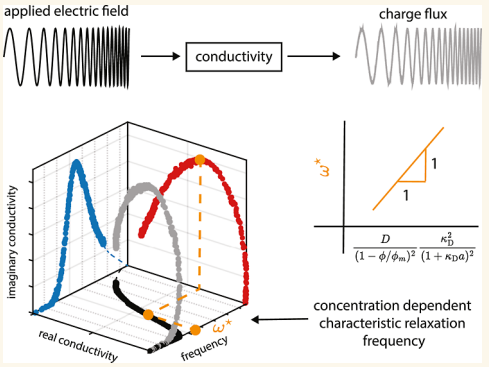

KEYWORDS: *concentrated electrolytes, nonequilibrium transport, charged nanoparticles, conductivity spectra, electrohydrodynamics*

The dynamic behavior of electrolyte or macroion solutions under an external electric field is crucial in a wide array of cutting-edge technologies, from water purification systems[1,2] to neuromorphic computing devices[3,4] and advanced sensors.[5] The motion of the ions (or macroions) in solution is quantified by specific conductivity, σ, which typically refers to the steady state response in a direct current (DC) measurement. However, contemporary applications such as memristors,[4,6] enhanced ion transport through carbon nanotubes,[7] and iontronic sensors[5] encompass dynamic processes that rarely reach steady state. As a result, relying on DC measurements proves inadequate to accurately guide the design of these sophisticated engineering systems. In these contexts, it is important to characterize charge flux through transient or alternating fields, which offer the unique advantage of revealing the temporal evolution of charge transport across varying time scales.

The response to slowly varying fields is governed by the long-time dynamics of ions, often exhibiting cooperative behavior in highly concentrated solutions.[8] In contrast, in the presence of rapidly changing fields, the focus shifts to the short-time dynamics, characterized by the instantaneous motion of ions. The response of ions to a time-varying field is typically encapsulated by the frequency-dependent conductivity, which offers insights into the interplay of these dynamic regimes

$$\sigma(\omega) = \hat{J}(\omega)/\hat{E}(\omega) \tag{1}$$

Here, $\hat{J}(\omega)$ represents the charge flux along the direction of the applied electric field, while $\hat{E}(\omega)$ denotes the corresponding electric field component. The hat symbol indicates a Fourier transform, defined as $\hat{f}(\omega) = \int f(t)\ \exp(-i\omega t)\ dt$, which transforms the function from the time domain into the frequency domain.

The analysis of dynamic frequency responses, including impedance measurements, traditionally relies on the application of oscillatory fields at fixed frequencies. The primary aim of this method is to quantify the electrolyte's motion captured by the charge flux within a controlled oscillatory state generated by an electric field, E, oscillating at a target angular

Received: October 7, 2024
Revised: March 27, 2025
Accepted: March 28, 2025
Published: April 7, 2025

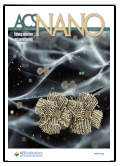

https://doi.org/10.1021/acsnano.4c14099
ACS Nano 2025, 19, 13673−13684

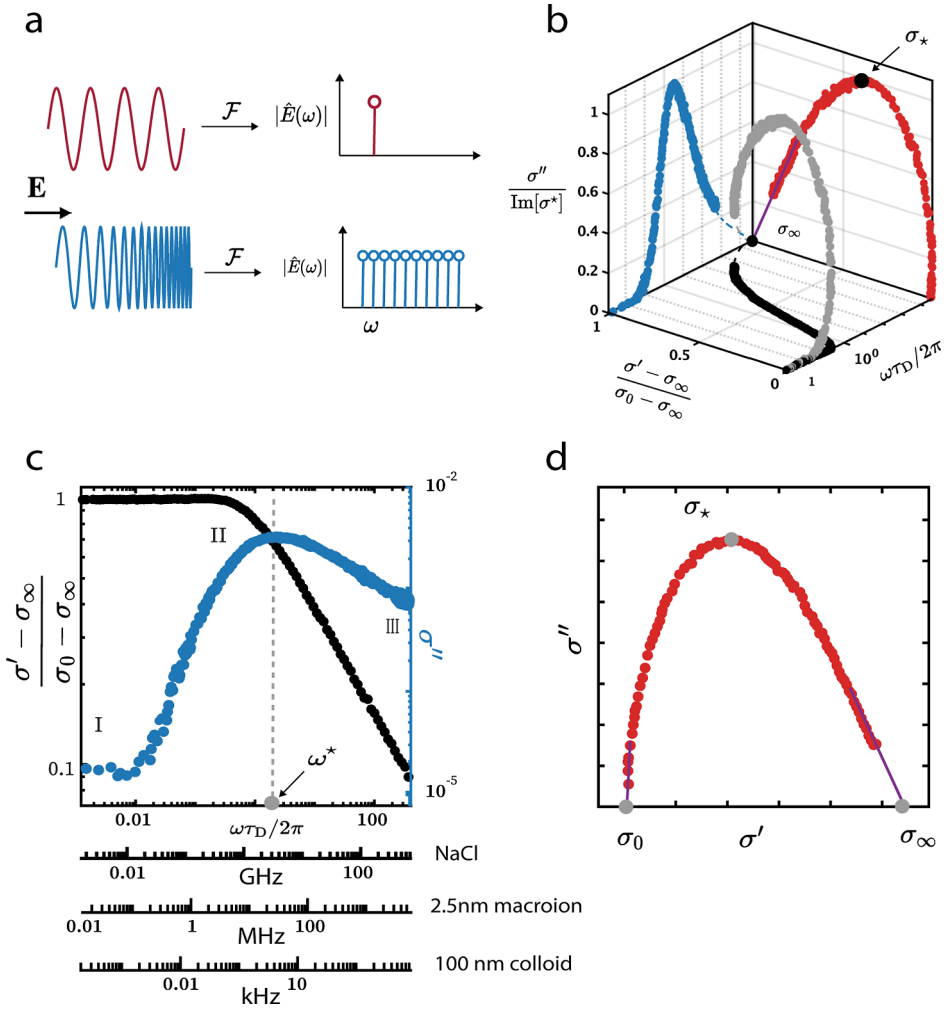

Figure 1. (a) (up) Diagram depicting a single tone applied field and that single tone excites the response at that particular frequency in the frequency spectrum. (bottom) An applied electric field whose frequency increases with time, known as a chirp signal, excites a range of frequencies as opposed to a single frequency. (b) 3D representation of dynamic conductivity as a function of the applied frequency in units of the ion diffusion time for a symmetric and binary electrolyte with $\varepsilon = \lambda_B/2a = 2.0$ and $\phi = 0.02$. Black, blue, and red markers depict the projections on the real, σ', imaginary, σ'', and frequency planes, respectively. (c) The projections of the frequency-dependent conductivity onto the real (black) and imaginary (blue) axes. The dashed gray line marks the crossover point between the real and imaginary contributions, denoted as the characteristic frequency of the suspension, ω^*. (d) An example of a Nyquist plot, illustrating the imaginary component (y axis) versus the real component (x axis) of the conductivity. The value corresponding to the characteristic frequency, ω^*, is labeled σ_*. The solid purple lines indicate the extrapolation to the zero-frequency conductivity, σ_0, and the infinite-frequency conductivity, σ_∞. Although this representation resembles an impedance spectrum, it only captures the contributions from the ions in the bulk phase.

frequency, ω_j. As shown schematically in subpanel (a) of Figure 1, the use of single-tone signals allows the excitation of only a single frequency at a time, thus capturing the system's response exclusively at that frequency. Consequently, a full spectrum frequency response necessitates conducting multiple experiments, each targeting a distinct frequency. Single-tone excitation signals are commonly used in impedance measurements.

While impedance measurements are a remarkably powerful tool, they are not without limitations, especially when used to determine bulk ionic conductivity. A key challenge lies in isolating the bulk response from phenomena associated with the electrodes in the electrochemical circuit.[9] Some examples of these phenomena are electrode polarization at low frequencies, which can significantly alter the local electric field, and, in consequence, ion dynamics,[10] and, electrode degradation,[11] which are not easily decoupled from the bulk ionic conductivity in impedance measurements.

Several theories have been proposed to describe the conductivity of electrolyte solutions. The most prominent expression for concentration-dependent steady-state conductivity is the Debye−Hückel-Onsager (DHO) model, which predicts a characteristic $n^{1/2}$ dependence, where n denotes the ion number density.[12,13] The DHO model, however, fails to provide reliable predictions at concentrations as low as a few hundred millimolar.[14] Mean-field frameworks for the frequency-dependent conductivity of symmetric and binary electrolytes often yield expressions of the form $\sigma(\omega) \sim 1/(1 - i(\omega\tau)^\zeta)$,[15−17] where τ is some characteristic relaxation time and $\zeta \in \mathbb{Z}$ is typically of magnitude equal or less than two. Nonetheless, due to mathematical complexity, these theories generally do not account for the finite, nonoverlapping volume of the charged species rendering them ill-equipped for accurately capturing the dynamic behavior of highly concentrated electrolytes.

https://doi.org/10.1021/acsnano.4c14099
ACS Nano 2025, 19, 13673−13684

Particle-based simulations have become a valuable tool for overcoming the limitations inherent to experimental measurements. Previous simulations investigating the dynamic conductivity of electrolyte solutions and macroions have predominantly focused on the response to varying field strengths in confined geometries, often neglecting interparticle hydrodynamic interactions.[18,19] Due to the mathematical and numerical complexities often present when simulating long-ranged and many-bodied interactions, such as electrostatic interactions, these studies have resorted to assuming pairwise electrostatic interactions and simulating small simulation boxes comprising only $O(10^2)$ ions. This simplification has been shown to underestimate conductivities when compared to experimental results.[20] These discrepancies underscore the necessity for more comprehensive modeling approaches that fully account for the coupled effects of electrostatic and hydrodynamic interactions in charged soft matter systems.

Here, we use nonequilibrium large-scale Brownian Dynamics simulations coupled with Poisson's equation to directly measure, as opposed to using Green−Kubo relations, the frequency-dependent ionic conductivity of symmetric and binary electrolytes (or macroions) in the presence of a time-varying electric field. Electrostatic and hydrodynamic interactions are handled through Spectrally accurate Ewald[21] and Positively Split Ewald summations,[22] thus including the many-bodied and long-raged hydrodynamic and electrostatic forces exerted on and by the charged particles relevant to the mesoscale. The solvent is assumed to behave as a Newtonian fluid with constant dielectric properties, and, consequently, does not capture the dielectric relaxation of common polar solvents at very high frequencies.

Moreover, in a significant departure from traditional single-tone methodologies, we propose employing an excitation signal inspired by the echolocation techniques of bats.[23] Bats utilize chirp signals, which modulate frequency upward or downward over time. An example of a chirp signal is depicted in blue at the bottom of Figure 1a. This signal design facilitates the excitation of a wide range of frequencies within a single electric field history protocol, thus allowing for a thorough examination of the system's frequency-dependent behaviors. To our knowledge, this approach has not been previously used in particle-based simulations of charged particles. Exponential chirp signals have proven to be highly effective in the viscoelastic characterization of soft gels, allowing accurate computation of the complete frequency spectrum at a much faster rate compared to traditional discrete frequency sweeps.[24,25]

RESULTS AND DISCUSSION

We employ exponential chirps, where the sine sweep maintains a constant amplitude while the frequency increases exponentially with time

$$E(t) = E_0 \sin((L\omega_1)(\exp(t/L) - 1)) \tag{2}$$

where E_0 is the amplitude of the applied field. The exponential growth of the signal phase from ω_1 to ω_2 is controlled by the time scale $L = t_f/\left(\log\left(\frac{\omega_2}{\omega_1}\right)\right)$, where $\log(x)$ represents the natural logarithm of x and t_f is the duration of the chirp signal. An example of this chirp signal is shown in blue in subpanel (a) of Figure 1. An example of the applied electric field in the form of a chirp is shown in Figure S1a. Applying this electric field induces an instantaneous charge flux, characterizing the response of the suspension as shown in Figure S1b. This methodology enables simultaneous probing of the electrolyte response across a range of frequencies, including nonlinear responses, thereby providing a more time-efficient history protocol and deeper insights into the charge transport mechanisms present in the time-dependent dynamics of charged suspensions.

As expressed in eq 1, the response of the charge flux to an applied electric field is governed by a complex conductivity, expressed as

$$\sigma(\omega) = \sigma'(\omega) + i\sigma''(\omega) \tag{3}$$

An example of this two-component conductivity is shown in Figure 1b in gray. Instead of visualizing frequency responses in three dimensions, they are typically represented as projections onto the real and imaginary planes, also shown in black and blue in Figure 1c. The crossover frequency between the real and imaginary components, denoted ω^*, identifies the characteristic frequency associated with the collective motion in the electrolyte (or macroion) solution. A straightforward strategy to determine the characteristic relaxation time of the suspension, $\sim 1/\omega^*$, is to find the frequency value that maximizes σ'' in the representation of the Nyquist plot, shown in Figure 1d. Nyquist plots are often used to display electrochemical impedance[26] and share some qualitative similarities with the measurements present in Figure 1d. Nevertheless, the Nyquist plots obtained in electrochemical impedance measurements often include additional features, such as electrode-specific resistance.[27] Our implicit solvent simulations provide the distinct advantage of directly measuring the bulk-ionic conductivity, offering a clearer picture into the material's intrinsic properties.

We delineate three distinct regions in the frequency response, as illustrated in Figure 1c:

1. Region I: at low frequencies, the conductivity is purely real. That is, ions respond instantaneously to the applied electric field.
2. Region II: as the frequency of oscillation increases, the charged species cannot keep pace, leading to phase lag. This results in an increase in the imaginary component of the complex conductivity, depicted in blue, and a corresponding decrease in the real component, shown in black.
3. Region III: at frequencies that exceed the characteristic relaxation time of the suspension, there is a decrease in the magnitudes of both the real and imaginary components of the conductivity.

In this work, we investigate the microscopic origins of the different dynamic regimes found in the frequency-dependent conductivity of semidilute and concentrated electrolytes or macroions. We begin by analyzing the limiting behaviors of conductivity as $\omega \to 0$ and $\omega \to \infty$. Second, we explain the microscopic origin of the changes in the conductivity at both regimes by looking at the partial pair correlation function of the ions and the mean square displacement of the charged species. Then, we propose a perturbation to the Maxwell−Wagner relaxation time that accounts for hydrodynamic and excluded volume interactions. Finally, we show that, when scaled on the inverse of this relaxation time, the frequency-dependent conductivity of semidilute and concentrated electrolytes/macroions collapses onto a master-curve.

https://doi.org/10.1021/acsnano.4c14099
ACS Nano 2025, 19, 13673−13684

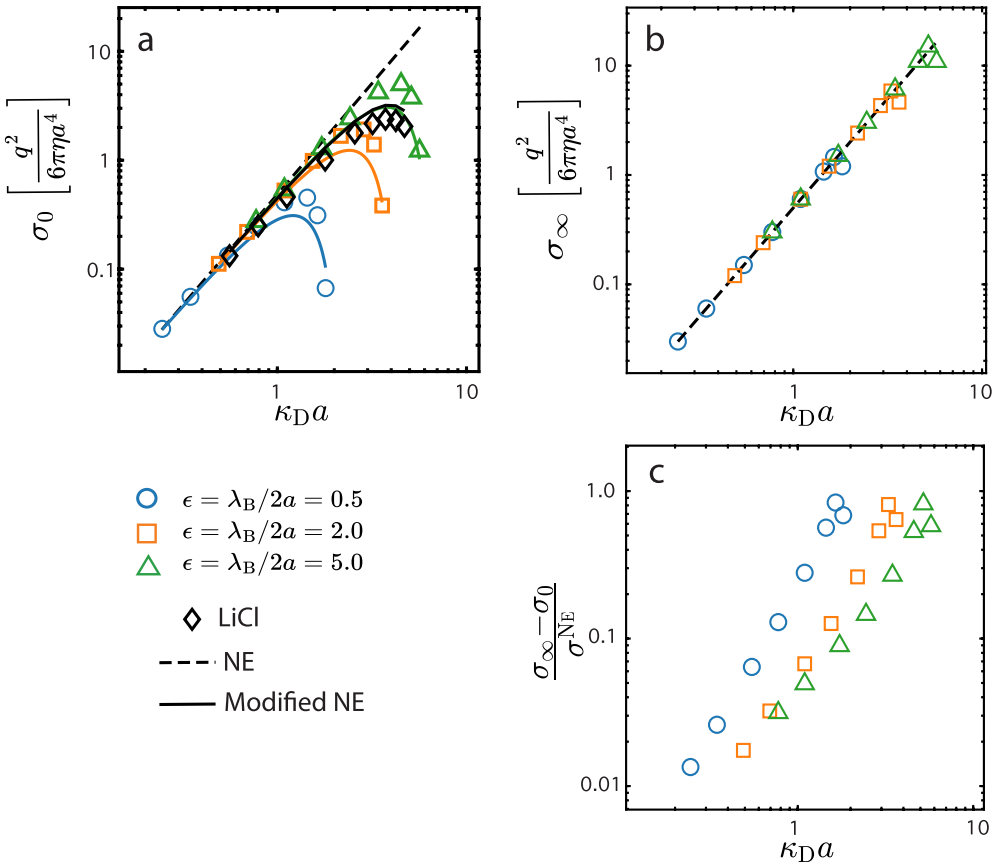

Figure 2. Computed (a) zero, σ_0, and (b) infinity, σ_∞, conductivities are shown as a function of the inverse Debye screening length in units of the particle's radius $\kappa_D a$. A dashed black line illustrates the theoretical conductivity for an ideal electrolyte solution corresponding to each ϵ. For reference, black markers indicate experimental measurements from ref 34. Solid lines in subpanel (a) correspond to corrected NE conductivities if $D \sim D_0^s(1 - \phi/\phi_m)^2$, where ϕ_m is the maximum packing fraction. (c) Increment of the conductivity. The lowest value for the coupling parameter, ϵ = 0.5, is shown by blue circle markers, ϵ = 2.0 for orange square markers, and ϵ = 5.0 for green triangle markers.

We compute the frequency-dependent conductivity using a transfer function[28] derived from the flux response in the direction of the field to overlapping chirps, where the lowest and highest sampled frequencies are $\omega\tau_D/2\pi = 0.001$ and $\omega\tau_D/2\pi = 400$, respectively. The representation in units of the diffusion relaxation time, $\tau_D = 6\pi\eta a^3/k_BT$, facilitates the exploration of the frequency response across a wide variety of charged soft matter systems. For example, our results are applicable to typical electrolytes, such as NaCl or LiCl in water at room temperature. Assuming an average hydrated ionic radius of $a \approx 0.5$ nm and a water viscosity of 1 cP, the diffusion relaxation time is estimated as $\tau_D \approx 0.6 \times 10^{-9}$ s. Consequently, the corresponding frequency range extends from $\omega = 0.0016$ GHz to $\omega = 660$ GHz. We note that the dynamic response of electrolyte solutions is commonly studied experimentally and computationally in the context of a complex permittivity (for example, see refs 29−31), including the dielectric relaxation of the solvent. Implicit-solvent simulations, however, are unable to capture important physical phenomena, such as the nonlinear dielectric response of water at frequencies exceeding 10 GHz.[32]

At the nanoscale, we turn our attention to macroions, which typically exhibit hydrated radii in the range 1−10 nm.[33] Assuming a representative radius of $a \approx 2.5$ nm for the simulated particles, the relaxation time becomes $\tau_D \approx 70 \times 10^{-9}$ s, corresponding to frequencies ranging from 0.01 to 5.5 $\times 10^3$ MHz. On the mesoscale, we consider charged colloids with radii of approximately $a \approx 100$ nm in water at room temperature. Here, the diffusion relaxation time is $\tau_D \approx 5$ ms, leading to a frequency range from $\omega = 0.2 \times 10^{-3}$ kHz to $\omega = 80 \times 10^3$ Hz. In all cases, the instantaneous charge density flux is evaluated at a rate at least four times greater than the highest applied frequency, ensuring sampling well above the standard Nyquist rate.

We control the charge of the particle, q, via the coupling parameter, ε (different from the permittivity of the solvent, ε_f). This quantity is related to the Bjerrum length, and we define it as the electric potential between two charges at contact with respect to the thermal energy

$$\varepsilon = \frac{q^2}{8\pi\varepsilon_f a k_B T} = \frac{\lambda_B}{2a} \tag{4}$$

where a is the hydrated radius of the ion and λ_B is the Bjerrum length. Notice that this is the effective electrostatic coupling constant, and thus can be used for atomic ions or nanoparticles. In what follows, we will refer to them as ions for simplicity, which we mean to encompass nanoparticles and macroions. The presented values of the electrostatic interactions relative to k_BT are chosen to be within the range of values commonly found in charged soft matter: $\varepsilon = [0.5, 2.0, 5.0]$. For example, for a solution of NaCl in water at room temperature, $\varepsilon \approx 1.1$ (assuming relative permittivity of 80). All distances are dimensionless on the radius of the hydrated ion/

https://doi.org/10.1021/acsnano.4c14099
ACS Nano 2025, 19, 13673−13684

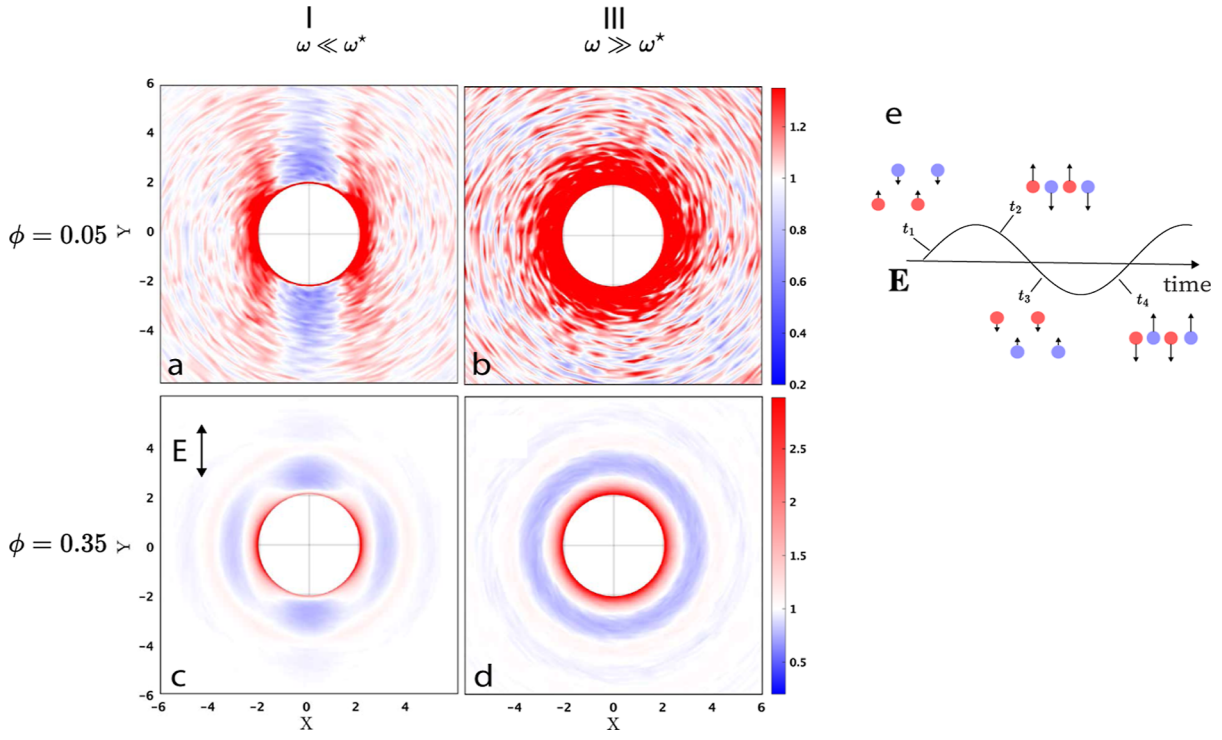

Figure 3. Diagrams of the computed radial correlation functions g_{+-} in the direction of extension (parallel to the applied electric field). The first and second columns correspond to the radial distributions sampled at frequencies $\omega/2\pi = 0.005\tau_D^{-1}$ and $\omega/2\pi = 200\tau_D^{-1}$, respectively. Subpanels a and b correspond to the semidilute regime with a total ion concentration of $\phi = 0.05$. Subpanels c and d correspond to the highly concentrated regime with $\phi = 0.35$. (e) Illustration of dynamic behavior leading to quadrupole distributions on the partial pair correlation functions in subpanels a and c.

macroion, a, and the time scale is set by the bare ion/macroion's Stokes−Einstein's relaxation time, $\tau_D = 6\pi\eta a^3/k_BT$, where η is the viscosity of the solvent.

First, we examine the limiting behaviors of regions I and III of the frequency spectrum, characterized by the zero- and infinite-frequency conductivities. These conductivities are closely linked to the dynamic diffusivity of the ions. Generally, we can distinguish at least three key translational diffusive processes for particles in suspension:[8] the short-time self-diffusivity (D_0^s), the long-time self-diffusivity (D_∞^s), and the gradient or collective diffusivity of the electrolyte. At infinite dilution, these values converge, reflecting uniform behavior across the system.

The long-time dynamic response of the electrolyte, governed by the long-time diffusivity, is reflected in the low-frequency regime, represented by $\sigma_0 = \lim_{\omega\to 0}\sigma(\omega)$. On the other hand, the high-frequency or short-time response, dictated by the short-time diffusivity, is captured by $\sigma_\infty = \lim_{\omega\to\infty}\sigma(\omega)$. Subpanels (a,b) of Figure 2 show the estimated limiting values $\sigma_0 = \lim_{\omega\to 0}\sigma(\omega)$ and $\sigma_\infty = \lim_{\omega\to\infty}\sigma(\omega)$, respectively, as a function of the inverse DH screening length $\kappa_D = \lambda_D^{-1}$. The DH screening length is given by $\lambda_D = \sqrt{\varepsilon_f k_B T/(e^2\sum_{a=1}^{M} n_\nu z_\nu^2)}$, where n_ν and z_ν are the bulk number density and valence of species ν respectively, e is the fundamental charge, ε_f is the solvent permittivity and k_BT is the thermal energy. For a symmetric electrolyte, the number density of ions, $n = n_+ + n_-$, is related to the volume fraction via $\phi = n(4\pi/3)a^3$. The conductivities shown in subpanels (a−c) of Figure 2 correspond to small electric fields ($E_0 = 0.1$ and $E_0 = 0.5$, in units of $k_BT/a^2\varepsilon_f$) and are independent of the strength of the applied electric field as demonstrated by Figure S2. Different colors in subpanels (a−c) of Figure 2 represent different values for the coupling parameters, $\varepsilon = \lambda_B/2a$. Blue markers indicate conductivities computed for weakly coupled samples with $\varepsilon = 0.5$, while green markers indicate the highly coupled regime, $\varepsilon = 5.0$, which is more representative of charged nanoparticles and macroions.[35] The volume fraction of the charged species, ϕ, is varied from 0.01 to 0.45, with increasing values along the positive direction of the horizontal axis.

In the dilute regime, we expect the computed values to converge toward the Nernst−Einstein specific conductivity, which, for a binary electrolyte, is defined as $\sigma^{NE} = nq^2(D_+ + D_-)$, where n is the number density of the ions. The dashed black line in Figure 2a represents this conductivity under the assumption that ions follow Stokes−Einstein self-diffusivity, $D = D_0^s = k_BT/6\pi\eta a$. For reasons that will be detailed later, at higher concentrations, we anticipate a significant decrease in the effective diffusivity of the ions with increasing concentration. The solid lines in Figure 2a depict the corrected NE conductivities obtained under the assumption that the effective diffusivity adheres to the relation $D \sim D_0^s(1 - \phi/\phi_m)^2$,[8] where ϕ_m represents the maximum packing fraction. In Figure 2a, the modified NE conductivity was obtained using the best fit for the maximum packing fraction, ϕ_m, constrained by close random packing at approximately 0.63 and hexagonal close packing at approximately 0.74.

In Figure 2a, we observe significant deviations from ideal solution behavior in σ_0 for $\phi \geq 0.05$. In contrast, such deviations are not as evident in extrapolated values of σ_∞ presented in Figure 2 b. The magnitude of $\Delta\sigma = \sigma_\infty - \sigma_0$, shown in subpanel (c) of Figure 2, in units of the Nernst−Einstein conductivity, σ^{NE} increases with ion concentration,

https://doi.org/10.1021/acsnano.4c14099
ACS Nano 2025, 19, 13673−13684

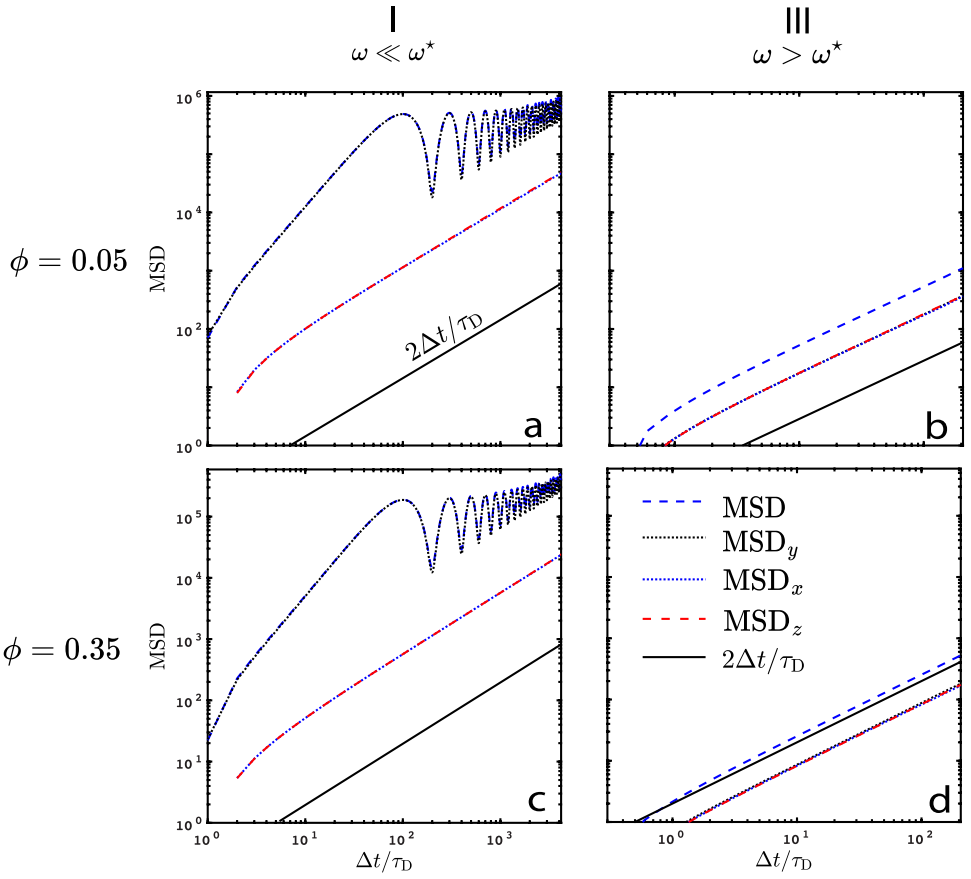

Figure 4. Ions mean square displacement (MSD) as a function of Δt. The first, second, and third columns correspond to displacements sampled at frequencies that correspond to region I ($\omega \ll \omega^*$), II($\omega < \omega^*$), and III ($\omega > \omega^*$), respectively. Subpanels a, b, and c correspond to the semidilute regime with a total ion concentration of ϕ = 0.05. Subpanels d, e, and f correspond to the highly concentrated regime with ϕ = 0.35. Notice the significant structural changes of the correlation function.

highlighting a concentration-dependent enhancement in the transport properties of the macroions. This growth $\Delta\sigma$ can be attributed to changes in the charge distribution of the ionic species in the low- and high-frequency regimes. Importantly, our findings indicate that the rate of change of $\Delta\sigma/\sigma^{NE}$ for concentrations $\phi < 0.35$ decreases with increasing ion−ion interaction strength or coupling parameter, ε. At higher concentrations, the computed values of $\Delta\sigma/\sigma^{NE}$ appear to be independent of the strength of the ion−ion interaction, ε. However, this behavior should be interpreted cautiously, as hydrodynamic lubrication interactions, which become increasingly significant in highly concentrated systems, are not accounted for in our simulations.

A straightforward approach to characterizing the structural properties of the ions is through pair distribution functions. The partial pair distribution function for a binary system is expressed as[36]

$$g_{\nu\mu}(\mathbf{r}) = \frac{1}{Vn_\nu n_\mu}\left\langle \sum_{\alpha=1}^{N_\nu} \sum_{\beta\neq\alpha}^{N_\mu} \delta(\mathbf{r} + \mathbf{r}_\alpha - \mathbf{r}_\beta)\right\rangle \tag{5}$$

where $\mathbf{r}_{\alpha/\beta}$ is the position of particle α of species ν or of particle β of species μ. In a single component system, particles α and β are by necessity of the same species; in a mixture, we can define the pair distribution function with ν and μ representing the same or different species. Figure 3 displays the partial pair distribution function for oppositely charged species, $g_{+,-}$, along the direction parallel to the applied field (the extensional direction). The first row represents the semidilute regime with ϕ = 0.05, while the second row shows a concentrated suspension with ϕ = 0.35. In Figure 3, columns (a,c) correspond to the single-tone frequency, $\omega/2\pi = 0.005\tau_D^{-1}$, and columns (b,d) correspond to $\omega/2\pi = 200\tau_D^{-1}$.

Here, we observe significant structural trends. In subpanel (a), the charge distribution function is symmetric around the extension axis, forming a quadrupole moment pattern along the direction of the field. This pattern, characterized by a zero-order symmetry, shows that oppositely charged species are more likely to align along the orthogonal direction, with a depletion region along the extensional axis. This arrangement results from the dynamic response of the ions to the applied field. Subpanel (e) in Figure 3 provides an illustrative (albeit simplified) depiction of the expected averaged trajectories for two pairs of oppositely charged ions. At early times of the oscillation period, t_1, the field exerts a force pushing positive ions along the field direction while negative ions move in the opposite direction. As the positive region of the oscillation progresses, t_2, positive and negative species approach close proximity, aligning along the orthogonal direction of the field. When the electric field reaches negative values, t_3, ions flip directions to meet again near the end of the oscillation cycle, t_4. This dynamic interaction accounts for the observed positive correlation between oppositely charged species along the orthogonal direction at low frequencies.

With increasing oscillation frequency (Figure 3b), the partial pair correlation function gradually loses its angular depend-

https://doi.org/10.1021/acsnano.4c14099
ACS Nano 2025, 19, 13673−13684

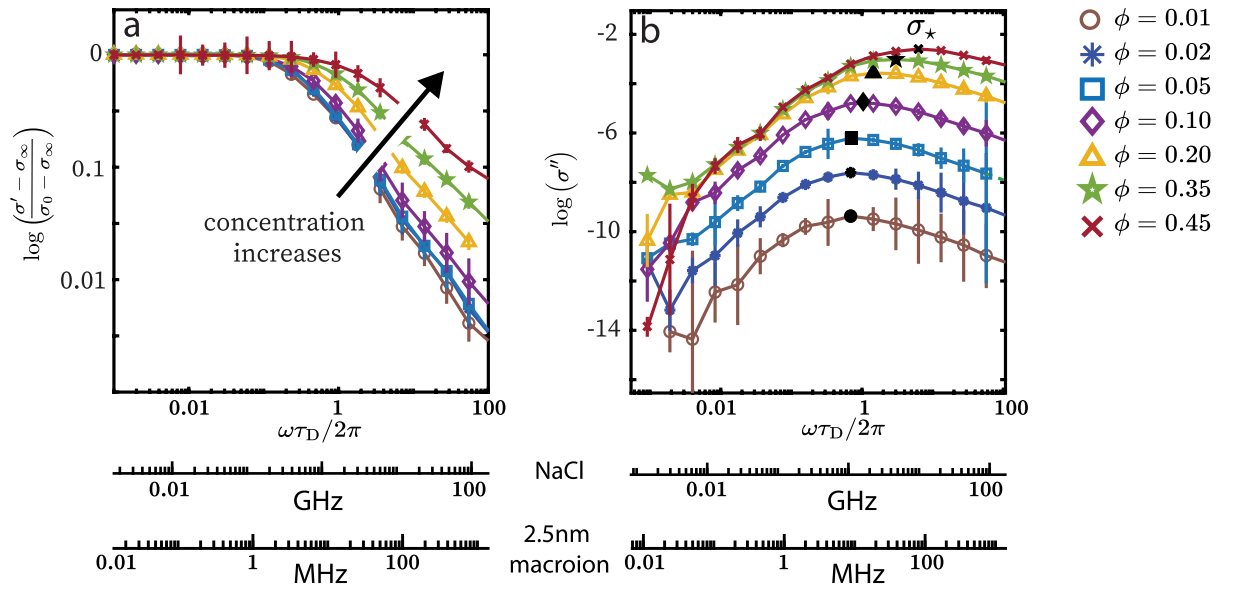

Figure 5. (a) Frequency response of the real contribution to the conductivity at different concentrations for E_0 = 0.5 in units of $k_BT/a^2\varepsilon_f$ and ε = 2.0. (b) Imaginary contribution to the frequency-dependent conductivity for E_0 = 0.5 in units of $k_BT/a^2\varepsilon_f$ and ε = 2.0. The Black markers indicate the location of the characteristic relaxation time of the suspension.

ence, approaching the pair distribution function observed in the absence of an electric field. This behavior arises because the ions lack sufficient time to respond to the rapidly oscillating field, restricting their motion to small distances and preventing perturbations to the charge distribution.

At higher concentrations, the partial pair correlation function develops a quadrupole pattern that is constrained by the neighboring shell. In this regime, the ions at equilibrium organize in a way that gives rise to charge waves.[37] This relevant structural feature is also present in the frequency response as shown by rings of ions distributed around the central particle. Consequently, at low frequencies and high concentrations, ion movement is impeded by the densely packed environment.[8] Conversely, at high frequencies, ions do not travel far enough to encounter significant spatial constraints. These structural features explain the increase in conductivity at high frequencies and why this increase becomes more pronounced with higher ionic concentration present in Figure 2c.

The differing dynamic response of the charged species at each of the frequency regimes can be further studied through the mean square displacement (MSD), $\langle(\mathbf{x}-\mathbf{x}(t))^2\rangle$. Panels a and b, alongside c and d in Figure 4, depict the MSD for concentrations of ϕ = 0.05 and ϕ = 0.35, respectively. In region I (subpanels a and c), where the oscillation frequency of the applied field approaches zero, the primary contributor to the MSD's magnitude (blue dashed line) is the transport of charged species in the field's direction, applicable to both the semidilute (first row) and concentrated (second row) regimes. Notably, the MSD oscillates every $200\tau_D$ at both high and low concentrations, corresponding to an applied field frequency of $0.005\tau_D^{-1}$. However, as concentration increases, the amplitude of these oscillations diminishes. This trend is anticipated because the neighboring cloud or cage must relax and rearrange to accommodate ion movement, thereby reducing the MSD.

At the highest frequency (second column of Figure 4), transport along the extensional axis (the direction of the field) relative to the orthogonal direction decreases. As oscillations occur on time scales below τ_D, only minor changes are observed, and diffusive transport is restored in both semidilute and concentrated regimes at larger time lags. Since diffusive transport is fundamental to the Nernst−Einstein equation, this observation aligns with the conductivity approaching the ideal value as $\omega \to \omega_\infty$. This underscores the profound influence of ion/nanoparticle packing on conductivity. At low frequencies and high concentrations, the behavior is largely dictated by long−range interactions and the collective motion of ions, resulting in deviations from ideal behavior. In contrast, at high frequencies, the response is chiefly driven by the short-range, immediate motion of ions, where the displacement is insufficient for packing effects to come into play.

For a more thorough analysis, details on the intermediate regions are needed. Therefore, we extract the frequency-dependent profile at different concentrations, strengths of ion−ion interactions, and applied electric fields, which ranged from E = 0.1 to E = 3.0 in units of $k_BT/a^2\varepsilon_f$. Example of the profiles obtained for the real and imaginary contributions are shown in Figure 5a,b, respectively. The real part of the conductivity σ' is rescaled by the range bounded by the zero-, $\sigma_0 = \lim_{\omega\to 0}\sigma(\omega)$, and ∞, $\sigma_\infty = \lim_{\omega\to\infty}\sigma(\omega)$ conductivities, $\Delta\sigma = \sigma_\infty - \sigma_0$; this is a common practice when characterizing the frequency response of other transport properties, such as the viscosity of a suspension.[38] The concentration increases moving upward, with the lowest concentration, ϕ = 0.01, represented by the brown circle markers, and the highest concentration, ϕ = 0.45, by the red X markers. As the concentration of the ions increases, important trends can be observed. For concentrations $\phi \leq 0.05$, depicted by circle, star, and square markers, the decay of the rescaled conductivity, in regions II and III, falls almost on the same line. However, at larger concentrations, the scaling of the decay decreases with increasing concentration.

Moreover, the characteristic relaxation time of the suspension shifts nonlinearly to the right as the concentration of charged species increases. This is most clearly observed in the imaginary contribution, shown in subpanel (b) of Figure 5, where the black markers indicate the values corresponding to

https://doi.org/10.1021/acsnano.4c14099
ACS Nano 2025, 19, 13673−13684

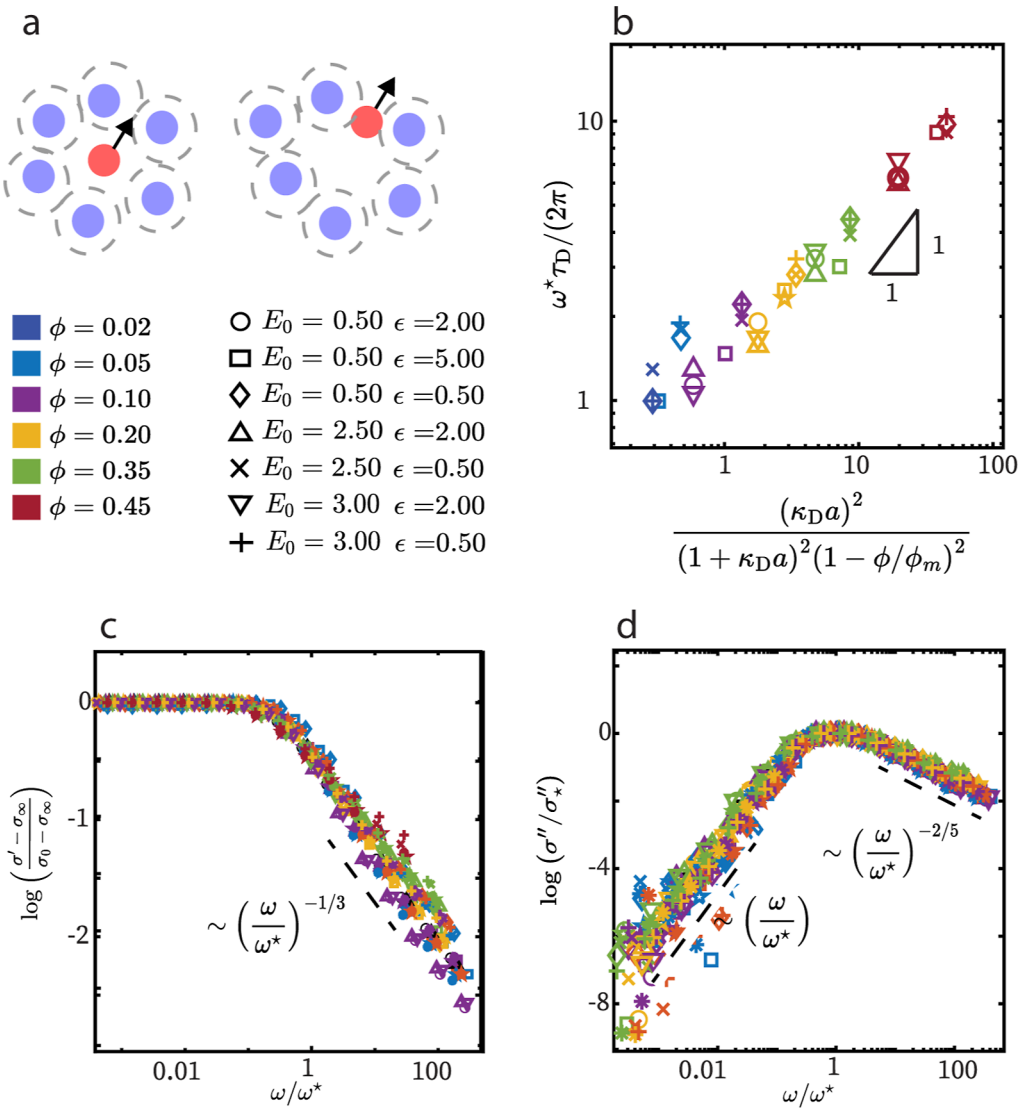

Figure 6. (a) A tracer particle, depicted in red, is encircled by neighboring particles, shown in blue, which form a cage-like structure. The tracer particle must await the relaxation of these neighboring particles before it can move beyond the confines of its cage. (b) The characteristic frequency, derived from the data, is presented as a function of the perturbed Maxwell−Wagner inverse relaxation time. The electric field is in units of $k_BT/a^2\epsilon_f$. (c) Real component of the conductivity as a function of the rescaled frequency. At frequencies greater than the characteristic frequency, the rescaled conductivity decays as $\sim(\omega/\omega^*)^{-1/3}$. (c) Imaginary contribution to the frequency-dependent conductivity as a function of the rescaled frequency. At frequencies below ω/ω^*, $\sigma'' \sim \omega/\omega^*$ and at frequencies above ω/ω^*, σ'' decays as $\sim(\omega/\omega^*)^{-2/5}$.

the characteristic frequency of the suspension. Importantly, the magnitude of the imaginary contribution to the conductivity increases with increasing concentration as expected. An explanation for this increase is that the ions must wait for their neighbors to rearrange and relax in response to the electric field, thus enhancing the magnitude of the imaginary contribution.

When it comes to characterizing the dynamic behavior of electrolytes, the choice of time scales is pivotal. Among the most established metrics are the Debye relaxation time, controlled by $\tau^{DH} = \lambda_D^2/D_0^s$, and the relaxation time linked to the Bjerrum length, $\tau^B = \lambda_B^2/D_0^s$. These time scales are typically benchmarked against the Stokes−Einstein diffusive time, a measure that reflects the diffusivity of a single-particle tracer. Consequently, regularization over these time scales is most accurate within the dilute regime.

In concentrated electrolytes, our findings suggest that there are two critical phenomena that govern the dynamics of the suspension. The first is the time scale over which ions change direction in response to a change in the electric field sign. The second is the time scale over which the ionic cloud or cage can relax. In the simplest terms, these competing processes can be understood as the relaxation of a dipole. In the presence of an electric field, the ionic cloud of a charged species will polarize with a charge separation distance l, approximately $O(a + \lambda_D)$. When the field direction is reversed, the dipole moment must change sign through diffusion and electromigration, requiring a time $O(l^2/D)$, where D is a characteristic ion diffusivity. Therefore, the time scale of the charge cloud at a frequency ω will coincide with the ionic transport time scales when $2\pi D\kappa_D^2/(1 + a\kappa_D)^2\omega \approx 1$, which is equivalent to the Debye relaxation time for $a = 0$.[35] This argument leads to what is

https://doi.org/10.1021/acsnano.4c14099
ACS Nano 2025, 19, 13673−13684

known in electrokinetics as the Maxwell−Wagner (MW) relaxation time and is commonly used in describing the dynamics of colloidal suspensions.

In contrast to the Debye relaxation time, MW relaxation time accounts for the size of the ion in the aforementioned dipole relaxation process, which becomes increasingly important at high concentrations. Nonetheless, Maxwell−Wagner theory assumes that an increase in ionic concentration will only perturb the size of the ionic cloud, here controlled by the Debye screening length, $\kappa_D^{-1} = \lambda_D$, without any hindrance from the dipole's cage. This ideality assumption is no longer valid in the concentrated regime, where excluded volume effects dominate the dynamics and, consequently, the effective diffusivity of the ions.

The inversion of the dipole sign suggests a diffusive mechanism operating at distances exceeding the ion diameter, indicating that the relevant time scale for the MW relaxation is governed by the long-time diffusivity. This diffusivity is intrinsically related to the diffusivity of a single particle, adjusted by an effective "size"—a factor determined by the density of neighboring particles or the "cage" that must be displaced for diffusion to occur. Consequently, the long-time diffusivity scales with the single-particle diffusivity, modulated by the radial distribution function at contact: $D^s_\infty \sim D^s_0/g(2a)$.[8] A diagram illustrating this process is shown in Figure 6a.

In the concentrated regime, electrostatic interactions are effectively screened at distances shorter than the ion diameter, leading to the dominance of excluded volume interactions in determining the effective particle size. When both excluded volume effects and interparticle hydrodynamic forces are considered, the effective diffusivity is expected to scale with $(1 - \phi/\phi_m)^2$, where ϕ_m is the maximum packing fraction.[8] Thus, we propose to scale the MW relaxation time on the long-time diffusivity time scale to account for this effective size

$$\omega^* \sim \frac{\omega^{MW}}{(1-\phi/\phi_m)^2} = \frac{D_0^s}{(1-\phi/\phi_m)^2}\frac{2\pi\kappa_D^2}{(1+\kappa_D a)^2} \tag{6}$$

where D^s_0 is the Stokes−Einstein diffusivity and ϕ_m the maximum packing fraction which we approximate as $\phi_m \approx 0.63$.

We estimated the characteristic relaxation time from the conductivity spectrum across a wide range of concentrations, ion−ion strength interaction, ε, and electric fields. The characteristic conductivity as a function of $\kappa_D^2/(1-\phi/\phi_m)^2(1+\kappa_D a)^2$ is shown in Figure 6b. We found such an approximation does exhibit the appropriate scaling for the characteristic relaxation time of the suspension for values of $\phi \geq 0.10$.

When scaled on this characteristic relaxation time, the real, σ', and imaginary, σ'', components of the complex conductivity at concentrations $\phi > 0.1$ fall on a universal curve as shown in Figure 6c,d. We also extract the scalings for the rate of increase and decrease of the imaginary contribution to the frequency-dependent conductivity. These are indicated by the dashed lines on the left-hand side and right-hand side of the characteristic frequency. We find the imaginary component of the conductivity increases linearly with the conductivity, as $(\omega/\omega^*)^{-2/5}$. The real contribution when scaled with respect to σ_∞ scales as $(\omega/\omega^*)^{-1/3}$ for frequencies above ω/ω^*.

CONCLUSION

In conclusion, this study provides a comprehensive analysis of the dynamic response of electrolyte/macroion solutions to time-varying electric fields, advancing our understanding of charge transport mechanisms across different frequencies and concentrations. By employing large-scale Brownian dynamics simulations coupled with Poisson's equation, we have elucidated the microscopic origins of various dynamic regimes in frequency-dependent conductivity. We have assumed that interparticle hydrodynamic interactions propagate instantaneously for an incompressible Newtonian fluid such that they can be captured by superposition of the hydrodynamic fields generated by a point particle and a point quadrupole using the RPY mobility tensor. Even in the absence of lubrication forces, which become increasingly important in the highly concentrated regime, our results reveal significant deviations from ideal behavior at low frequencies and high concentrations, highlighting the influence of ion packing and collective motion on charge transport.

We identified three main regions in the frequency response, each characterized by distinct transport mechanisms: instantaneous response at low frequencies, increased lagging and imaginary contribution at intermediate frequencies, and diminished conductivity at high frequencies. The use of chirp signals allowed us to probe a broad range of frequencies, offering a more detailed picture of the electrolyte's behavior compared to traditional single-tone signals.

Importantly, our analysis shows that the characteristic relaxation time, influenced by ion−ion interactions and concentration, plays a critical role in determining the frequency response. At frequencies below the characteristic dielectric relaxation time of the solvent molecules (approximately 10 GHz for water),[32] the proposed modified MW relaxation time accounts for excluded volume effects and provides a robust framework for predicting the dynamic response of concentrated electrolytes and charged macromolecules.

In essence, this work not only enhances our fundamental understanding of ion transport in electrolytes, macroions, and charged nanoparticles in solution but also offers practical insights for optimizing applications ranging from neuromorphic computing to advanced sensor technologies. The findings underscore the need to consider dynamic regimes and collective effects in designing systems that leverage the complex behavior of electrolytes under time-varying fields.

METHODS

Brownian Dynamics. We represent the ions in the electrolyte as a collection of charged, rigid, spherical particles suspended in solution. The solvent, treated implicitly, behaves as a Newtonian fluid, interacting with the ions through forces generated by hydrodynamic flows and stochastic Brownian forces driven by the momentum relaxation of solvent molecules.[39] At the ion scale, inertial relaxation happens on time scales vastly shorter than the time required for ion movement. In this regime, any disturbance to ion momentum is nearly instantaneous, causing the ion to quickly reach its terminal velocity. This allows us to disregard inertia entirely. Under these conditions, the ion dynamics are governed by the overdamped Langevin equation

$$0 = \mathbf{F}^H_\alpha + \mathbf{F}^I_\alpha + \mathbf{F}^E_\alpha + \mathbf{F}^B_\alpha \tag{7}$$

where $\mathbf{F}^H_\alpha$ is the hydrodynamic force acting on the α^{th} ion, $\mathbf{F}^I_\alpha$ accounts for forces arising from a generic conservative potential, $\mathbf{F}^E_\alpha$ is the external force exerted by a global field[21] and $\mathbf{F}^B_\alpha$ is the stochastic,

https://doi.org/10.1021/acsnano.4c14099
ACS Nano 2025, 19, 13673−13684

Brownian force. The last force satisfies the fluctuation−dissipation theorem[35] with ensemble average

$$\langle \mathbf{F}^{\mathrm{B}}(t)\rangle = 0; \qquad \langle \mathbf{F}^{\mathrm{B}}(t)\mathbf{F}^{\mathrm{B}}(t+\tau)\rangle = 2k_{\mathrm{B}}T(\mathbf{M}^{\mathrm{H}})^{-1}\delta(\tau) \tag{8}$$

where $\mathbf{F}^{B}(t) = [\mathbf{F}_1^{B}(t),\mathbf{F}_2^{B}(t),\cdots]$, $\langle\cdot\rangle$ indicates the expectation value, δ is the Dirac delta function and $\mathbf{M}^{\mathrm{H}}$ is the hydrodynamic mobility tensor. This approach guarantees that any energy an ion acquires from thermal fluctuations is rapidly dissipated as drag into the surrounding solvent.

To account for interparticle hydrodynamic interactions, we employ the Rotne−Prager−Yamakawa (RPY) tensor[40]

$$\mathbf{M}^{\mathrm{H}}_{\alpha\beta} = \frac{1}{\gamma}\begin{cases}\left(\frac{3a}{4r} + \frac{a^3}{2r^3}\right)\mathbf{I} + \left(\frac{3a}{4r} - \frac{2a^3}{2r^3}\right)\hat{\mathbf{r}}\hat{\mathbf{r}}, & r > 2a\\ \left(1 - \frac{9r}{32a}\right)\mathbf{I} + \left(\frac{3r}{32a}\right)\hat{\mathbf{r}}\hat{\mathbf{r}}, & r \le 2a\end{cases} \tag{9}$$

This expression captures the hydrodynamic coupling between particles, where $\mathbf{M}^{\mathrm{H}}_{\alpha\beta}$ represents the mobility tensor, modulating the relative motion of two particles as a function of their separation distance, r.

The hydrodynamic mobility tensor couples the nonhydrodynamic force, $\mathbf{F}_\beta = \mathbf{F}^{\mathrm{I}}_\beta + \mathbf{F}^{\mathrm{E}}_\beta + \mathbf{F}^{\mathrm{B}}_\beta$, to the velocity of the α^{th} ion

$$\mathbf{u}_\alpha(t) = \sum_{\beta=1}^{N} \mathbf{M}^{\mathrm{H}}_{\alpha\beta}\cdot\mathbf{F}_\beta(t) \tag{10}$$

Equation 7 can be numerically solved via an Euler−Maruyama integration scheme

$$\mathbf{x}_\alpha(t+\Delta t) = \mathbf{x}_\alpha(t) + \mathbf{u}_\alpha(t)\Delta t \tag{11}$$

where Δt is the time step over which ion trajectories are advanced. Additional details on the simulation of hydrodynamically interacting particles is found in ref 22.

Forces arising from conservative interactions among ions are represented as the gradient of a potential energy $U(\mathcal{X})$, which is a function of the coordinates of all ions $\mathcal{X} \equiv [\mathbf{x}_1, \mathbf{x}_2, ..., \mathbf{x}_N]^T$

$$\mathbf{F}^{\mathrm{I/E}}_\alpha(\mathcal{X}) \equiv -\nabla_{\mathbf{x}_\alpha} U^{\mathrm{I/E}}(\mathcal{X}) \tag{12}$$

where the gradient is taken with respect to the position of the α^{th} particle.

In our analysis, we consider finite-sized ions that inherently cannot overlap. To manage hard-core repulsion, we implement the Heyes and Melrose "potential-free" hard sphere algorithm,[41] which temporarily allows particle overlap due to external forces during a time step, then re-establishes contact by the end. Given that eqs 10 and 11 provide a map between particle displacements and forces, we are able to determine the force needed to reposition two overlapping ions into contact after a time step. Thus, the potential-free algorithm effectively translates into a hard sphere pair potential for particles that interact hydrodynamically through the RPY tensor as[38]

$$U^{\mathrm{hs}}_{\alpha\beta}(r) = \begin{cases}\frac{8\gamma}{3\Delta t}\left(2a\,\log\left(\frac{2a}{r}\right) + r - 2a\right) & \text{if } r < 2a\\ 0 & \text{if } r \ge 2a\end{cases} \tag{13}$$

where a_{hs} is the effective hard sphere radius of an ion, which can be different from the radius of the shell over which the ion's charge is distributed, a. In the form of the potential used here, γ and a_{hs} are the same for all particles. The total potential energy due to the hard sphere repulsion can be decomposed into a sum of pair potentials $U_{\alpha\beta}$

$$U^{\mathrm{hs}}(\mathcal{X}) = \frac{1}{2}\sum_{\alpha,\beta} U^{\mathrm{hs}}_{\alpha\beta}(|\mathbf{x}_\alpha - \mathbf{x}_\beta|) \tag{14}$$

where α and β indices run over all particles, and the factor of 1/2 corrects for double-counting each pair.

Charged species experience additional electrostatic forces, which are determined by solving Poisson's equation for the scalar potential, $\psi(\mathbf{x})$.[42,43] In our approach, we regularize the potential near an ion by distributing its charge across a spherical shell with radius a. This arrangement ensures that all free charge resides on this surface, thereby reducing Poisson's equation to Laplace's equation for the potential both outside and inside each ion shell

$$\nabla^2\psi = 0 \tag{15}$$

with boundary conditions on the shell of ion α given by

$$\psi_{\mathrm{p}} = \psi_{\mathrm{f}}, \qquad (\mathbf{E}_{\mathrm{f}} - \mathbf{E}_{\mathrm{p}})\cdot\hat{\mathbf{n}} = q_\alpha/(4\pi a^2) \tag{16}$$

here, ψ_{p} and ψ_{f} denote the potentials inside and outside the shell, respectively. The expression for the uniform free surface charge density on a spherical shell of radius a for ion α with net charge q_α is given by $\frac{q_\alpha}{4\pi a^2}$. The vector $\hat{\mathbf{n}}$ indicates the outward normal, while $\mathbf{E}_{\mathrm{f}}$ and $\mathbf{E}_{\mathrm{p}}$ represent the electric fields outside and inside the particle, respectively.[42,43] As ions move or external fields vary, the boundary conditions in eq 16 evolve over time. Thus, the introduction of time-dependence into Laplace's equation occurs solely through these time-varying boundary conditions, making the electric potential equations pseudosteady.

Starting from the integral form of Laplace's equation for the electric potential in the fluid and employing a multipole expansion on the ion surfaces as detailed in ref 21 we establish a connection between the moments of particles and fluid. This enables the construction of a system of equations in the following form

$$\langle\Psi\rangle - \Psi_0 = \mathcal{M}^{E}_{\Psi q}\cdot Q \tag{17}$$

where on the left-hand side of the equation $\langle\Psi\rangle - \Psi_0 = [\langle\psi_1\rangle - \psi_0(\mathbf{x}_1), \langle\psi_2\rangle - \psi_0(\mathbf{x}_2), ..., \langle\psi_N\rangle - \psi_0(\mathbf{x}_N)]^T$ is a list of the relative potentials for each of the ions, ψ_0 being the externally imposed potential field at the ion center and $\langle\psi_\alpha\rangle$ being the surface averaged potential of the α^{th} ion. On the right-hand side, $Q = [q_1, q_2, ..., q_N]$ is the list of ion charges, and $\mathcal{M}^{E}_{\Psi q}$ is known as the potential matrix.

The potential-charge coupling in $\mathcal{M}^{E}_{\Psi q}$ between ions α and β is given by

$$\frac{1}{\varepsilon_{\mathrm{f}} V}\sum_{\mathbf{k}\neq 0} j_0^2(ka)\frac{e^{i\mathbf{k}\cdot(\mathbf{x}_\alpha - \mathbf{x}_\beta)}}{k^2} \tag{18}$$

this interaction is akin to a Coulomb-type interaction but is regularized for ion centers closer than $2a$. Computing elements like those in eq 18 is computationally intensive, as the summand decays as $\frac{1}{k^4}$ and requires a substantial number of terms to achieve convergence. To enhance computational efficiency, we employ the Spectral Ewald method, as described in ref 21. This technique allows for the calculation of ion potentials from their charges with log−linear computational complexity, facilitating rapid simulations of up to $O(10^5)$ ions in this study. The total electric potential energy of the electrolyte is

$$U^{\mathrm{E}} = \frac{1}{2}Q\cdot(\langle\Psi\rangle - \Psi_0) \tag{19}$$

By employing eq 17 and computing the gradient of the electric potential energy, we can determine the electric force exerted on the α^{th} particle

$$\mathbf{F}^{\mathrm{E}}_\alpha = -\sum_\beta \nabla_{\mathbf{x}_\beta}\mathcal{M}^{E}_{\psi q} q_\alpha q_\beta \tag{20}$$

This force is determined using the same matrix-free techniques as those applied to the potential in ref 21. The simulations were performed in HOOMD-Blue.[44]

https://doi.org/10.1021/acsnano.4c14099
ACS Nano 2025, 19, 13673−13684

ASSOCIATED CONTENT

Supporting Information

The Supporting Information is available free of charge at https://pubs.acs.org/doi/10.1021/acsnano.4c14099.

Additional details on the applied chirp signal. Table summarizing simulation parameters. Figure S1a example of the applied electric field as a function of time. Figure S1b computed charge flux as a function of time. Figure S2 zero-frequency conductivity for small electric fields as a function of the inverse Debye screening length (PDF)

AUTHOR INFORMATION

Corresponding Author

Emily Krucker-Velasquez − *Department of Chemical Engineering, Massachusetts Institute of Technology, Cambridge, Massachusetts 02139, United States;* orcid.org/0000-0002-0531-1970; Email: ekrucker@mit.edu

Authors

Martin Z. Bazant − *Department of Chemical Engineering, Massachusetts Institute of Technology, Cambridge, Massachusetts 02139, United States;* orcid.org/0000-0002-8200-4501

Alfredo Alexander-Katz − *Department of Materials Science and Engineering, Massachusetts Institute of Technology, Cambridge, Massachusetts 02139, United States*

[§]**James W. Swan** − *Department of Chemical Engineering, Massachusetts Institute of Technology, Cambridge, Massachusetts 02139, United States*

Complete contact information is available at: https://pubs.acs.org/10.1021/acsnano.4c14099

Notes

The authors declare no competing financial interest.

[§]Deceased Nov, 2021.

ACKNOWLEDGMENTS

We thank the support from NASA, grant no. 80NSSC18K0162 and NSF, Career Award no. 1554398.

REFERENCES

(1) Chen, L.; Yin, Z.; Li, F.; Chen, Z. Treatment of Simulated Saline Brine Water by Membrane Distillation Process Enhanced Through Alternating Current Electric Field. *Chem. Eng. Res. Des.* **2023**, *192*, 167−179.

(2) Alkhadra, M. A.; Conforti, K. M.; Gao, T.; Tian, H.; Bazant, M. Z. Continuous Separation of Radionuclides from Contaminated Water by Shock Electrodialysis. *Environ. Sci. Technol.* **2020**, *54*, 527−536.

(3) Robin, P.; Kavokine, N.; Bocquet, L. Modeling of Emergent Memory and Voltage Spiking in Ionic Transport Through Angstrom-Scale Slits. *Science* **2021**, *373*, 687−691.

(4) Noy, A.; Li, Z.; Darling, S. B. Fluid Learning: Mimicking Brain Computing with Neuromorphic Nanofluidic Devices. *Nano Today* **2023**, *53*, 102043.

(5) Boahen, E. K.; Pan, B.; Kweon, H.; Kim, J. S.; Choi, H.; Kong, Z.; Kim, D. J.; Zhu, J.; Ying, W. B.; Lee, K. J.; Kim, D. H. Ultrafast, Autonomous Self-Healable Iontronic Skin Exhibiting Piezo-Ionic Dynamics. *Nat. Commun.* **2022**, *13*, 7699.

(6) Mao, L. Neuromorphic Sensing: A New Breed of Intelligent Sensors. *ACS Sens.* **2023**, *8*, 2896−2897.

(7) Shkodra, B.; Petrelli, M.; Angeli, M. A. C.; Garoli, D.; Nakatsuka, N.; Lugli, P.; Petti, L. Electrolyte-Gated Carbon Nanotube Field-Effect Transistor-Based Biosensors: Principles and Applications. *Appl. Phys. Rev.* **2021**, *8*, 041325.

(8) Brady, J. F. The Long-Time Self-Diffusivity in Concentrated Colloidal Dispersions. *J. Fluid Mech.* **1994**, *272*, 109−134.

(9) Vivier, V.; Orazem, M. E. Impedance Analysis of Electrochemical Systems. *Chem. Rev.* **2022**, *122*, 11131−11168.

(10) Jiménez-Ángeles, F.; Ehlen, A.; Olvera de la Cruz, M. Surface Polarization Enhances Ionic Transport and Correlations in Electrolyte Solutions Nanoconfined by Conductors. *Faraday Discuss.* **2023**, *246*, 576−591.

(11) Zhuang, D.; Bazant, M. Z. Population Effects Driving Active Material Degradation in Intercalation Electrodes. *Phys. Rev. E* **2023**, *107*, 044603.

(12) Debye, P.; Hückel, E. Zur Theorie der Elektrolyte: Gefrierpunktserniedrigung und Verwandte Erscheinungen. *Phys. Z.* **1923**, *24*, 185−206.

(13) Onsager, L. Zur Theorie der Elektrolyte. I. *Z. Phys.* **1926**, *27*, 388.

(14) Avni, Y.; Andelman, D.; Orland, H. Conductance of Concentrated Electrolytes: Multivalency and the Wien Effect. *J. Chem. Phys.* **2022**, *157*, 154502.

(15) Israelachvili, J. N. *Intermolecular and Surface Forces*, 3rd ed.; Academic Press: Waltham, MA, 2011.

(16) Chandra, A.; Bagchi, B. Frequency Dependence of Ionic Conductivity of Electrolyte Solutions. *J. Chem. Phys.* **2000**, *112*, 1876−1886.

(17) Bonneau, H.; Avni, Y.; Andelman, D.; Orland, H. Frequency-Dependent Conductivity of Concentrated Electrolytes: A Stochastic Density Functional Theory. *J. Chem. Phys.* **2024**, *161*, 244501.

(18) Hoang Ngoc Minh, T.; Stoltz, G.; Rotenberg, B. Frequency and Field-Dependent Response of Confined Electrolytes from Brownian Dynamics Simulations. *J. Chem. Phys.* **2023**, *158*, 104103.

(19) Pireddu, G.; Rotenberg, B. Frequency-Dependent Impedance of Nanocapacitors from Electrode Charge Fluctuations as a Probe of Electrolyte Dynamics. *Phys. Rev. Lett.* **2023**, *130*, 098001.

(20) Panagiotopoulos, A. Z.; Yue, S. Dynamics of Aqueous Electrolyte Solutions: Challenges for Simulations. *J. Phys. Chem. B* **2023**, *127*, 430−437.

(21) Krucker-Velasquez, E.; Swan, J. W.; Sherman, Z. Immersed Boundary Method for Dynamic Simulation of Polarizable Colloids of Arbitrary Shape in Explicit Ion Electrolytes. *J. Chem. Phys.* **2024**, *161*, 164110.

(22) Fiore, A. M.; Balboa Usabiaga, F.; Donev, A.; Swan, J. W. Rapid Sampling of Stochastic Displacements in Brownian Dynamics Simulations. *J. Chem. Phys.* **2017**, *146*, 124116.

(23) Pye, D. Echolocation Signals of Bats: A Retrospective. *Bioacoustics* **2021**, *30*, 487−497.

(24) Bouzid, M.; Keshavarz, B.; Geri, M.; Divoux, T.; Del Gado, E.; McKinley, G. H. Computing the Linear Viscoelastic Properties of Soft Gels Using an Optimally Windowed Chirp Protocol. *J. Rheol.* **2018**, *62*, 1037−1050.

(25) Geri, M.; Keshavarz, B.; Divoux, T.; Clasen, C.; Curtis, D. J.; McKinley, G. H. Time-Resolved Mechanical Spectroscopy of Soft Materials via Optimally Windowed Chirps. *Phys. Rev. X* **2018**, *8*, 041042.

(26) Effendy, S.; Song, J.; Bazant, M. Z. Analysis, Design, and Generalization of Electrochemical Impedance Spectroscopy (EIS) Inversion Algorithms. *J. Electrochem. Soc.* **2020**, *167*, 106508.

(27) Lazanas, A. C.; Prodromidis, M. I. Electrochemical Impedance Spectroscopy: A Tutorial. *ACS Meas. Sci. Au* **2023**, *3*, 162−193.

(28) Proakis, J. G.; Manolakis, D. G. *Digital Signal Processing: Principles, Algorithms, and Applications*, 3rd ed.; Prentice Hall: Upper Saddle River, NJ, 1996.

(29) Śmiechowski, M.; Sun, J.; Forbert, H.; Marx, D. Solvation Shell Resolved THz Spectra of Simple Aqua Ions: Distinct Distance- and Frequency-Dependent Contributions of Solvation Shells. *Phys. Chem. Chem. Phys.* **2015**, *17*, 8323−8329.

(30) Buchner, R.; Hefter, G. Interactions and Dynamics in Electrolyte Solutions by Dielectric Spectroscopy. *Phys. Chem. Chem. Phys.* **2009**, *11*, 8984.
(31) Rinne, K. F.; Gekle, S.; Netz, R. R. Dissecting Ion-Specific Dielectric Spectra of Sodium-Halide Solutions into Solvation Water and Ionic Contributions. *J. Chem. Phys.* **2014**, *141*, 214502.
(32) Buchner, R.; Barthel, J.; Stauber, J. The Dielectric Relaxation of Water Between 0°C and 35°C. *Chem. Phys. Lett.* **1999**, *306*, 57−63.
(33) Liu, Z.; Liu, T.; Tsige, M. Elucidating the Origin of the Attractive Force Among Hydrophilic Macroions. *Sci. Rep.* **2016**, *6*, 26595.
(34) *CRC Handbook of Chemistry and Physics*, 70th ed.; Weast, R. C., Ed.; CRC Press: Boca Raton, FL, 1989
(35) Saville, D. A.; Russel, W. B.; William, R. *Colloidal Dispersions; Cambridge Monographs on Mechanics*; Cambridge University Press: Cambridge, UK, 1989.
(36) Hansen, J.-P.; McDonald, I. R. *Theory of Simple Liquids: With Applications to Soft Matter*, 4th ed.; Elsevier: Amstersdam, 2013.
(37) Krucker-Velasquez, E.; Swan, J. W. Underscreening and Hidden Ion Structures in Large-Scale Simulations of Concentrated Electrolytes. *J. Chem. Phys.* **2021**, *155*, 134903.
(38) Varga, Z.; Swan, J. W. Linear Viscoelasticity of Attractive Colloidal Dispersions. *J. Rheol.* **2015**, *59*, 1271−1298.
(39) Frenkel, D.; Smit, B. *Understanding Molecular Simulation: From Algorithms to Applications*, 2nd ed.; Academic Press: San Diego, CA, 2002.
(40) Kim, S.; Karrila, S. J. *Microhydrodynamics: Principles and Selected Applications*; Dover Publications: Mineola, NY, 2005.
(41) Heyes, D. M.; Melrose, J. R. Brownian Dynamics Simulations of Model Hard-Sphere Suspensions. *J. Non-Newtonian Fluid Mech.* **1993**, *46*, 1−28.
(42) Jackson, J. D. *Classical Electrodynamics*, 3rd ed.; Wiley: Hoboken, NY, 2009
(43) Landau, L. D.; Lifshits, E. M.; Pitaevskiĭ, L. P.; Sykes, J. B.; Bell, J. S.; Kearsley, M. J. *Electrodynamics of Continuous Media*, 2nd ed.; Elsevier Butterworth-Heinemann: Amsterdam, 2009.
(44) Anderson, J. A.; Glaser, J.; Glotzer, S. C. HOOMD-Blue: A Python Package for High-Performance Molecular Dynamics and Hard Particle Monte Carlo Simulations. *Comput. Mater. Sci.* **2020**, *173*, 109363.

https://doi.org/10.1021/acsnano.4c14099
ACS Nano 2025, 19, 13673−13684